A frequency-limited waviness and curvature measurement algorithm for composite fibre trackings

Adrià Julià i Juanola, Marc Ruiz i Altisent, Narcís Coll i Arnau, Imma Boada i Oliveras *

Graphics and Imaging Laboratory (GILAB), Universitat de Girona, Edifici P-IV, 17001 Girona, Catalonia, Spain

ARTICLE INFO

ABSTRACT

Given a set of irregularly sampled 3D polygonal curves representing composite fibres within a micro-computed tomography volume, a new approach based on the Frenet–Serret formulas is proposed to measure the point curvature and waviness along a polyline even when its oscillations are not coplanar. However, a direct computation of the measures would lead to ill-formed results depending on variant externalities across acquisitions such as noise, sampling, resolution, fractality, etc. Consequentially, we also propose a decoupling mechanism employing a low-pass Gaussian frequency filter to gradually discard features smaller than a certain user-specified σ wavelength referenced in actual space units. This proposal has been tested, characterized and visualized using both real and synthetic datasets contemplating complex waveform features to assess the filter selectivity and convergence across varying sampling frequencies (i.e. polyline resolution). The C++ *VTK* implementation, alongside an extra amount of supplementary materials encompassing the execution results and synthetic datasets is provided.

1. Introduction

In the last years, 3D X-ray micro-computed tomography (μCT) has become an extensively used technique in materials science as is able to non-destructively capture detailed and precise information of materials composition as a stack of X-ray CT images defining a three-dimensional volume [1,2]. Depending on the use case, in order to explore and obtain information from these volumetric datasets, specific methods have to be designed; a design that can be challenging depending on the application, specially, when pure 3D-based approaches want to be considered. In this paper, our interest has been focused on the quantification of fibre waviness: a geometrical defect in fibre reinforced polymer composites with direct implications on mechanical properties as exposed in reviews such as [3,4].

Generally, fibre waviness evaluation methods consider a μCT input volume, and analyse it with a two step process, where first, an approximation of the fibres is obtained and then measurements over the reconstructed fibre orientations are performed. They define (or implicitly assume) a set of cutting planes over the μCT volume, ideally, perpendicularly oriented to the principal fibre directions. Then, some evaluate the fibre sections which will be circular in case of normally aligned fibres and elliptical otherwise [5,6]. This is usually complemented by the more generalist approach of detecting the centres and then knitting or correlating them between slices in order to obtain their

in-plane (the deviation of fibre from the normal fibre direction in a plane of the lamina) and out-plane (bending of a single or multiple fibre separated from the laminate fibrous layer) deviations [7–14]. There are also alternative methods such as [15,16] capable of reconstructing fibres. Other approaches quantify the waviness directly at every voxel avoiding the complexities of producing polygonal fibre trackings. These voxel-based methods, generally, after a fibre segmentation process, analyse the neighbourhood around each voxel using kernels and applying the tensor or similar strategies in order to obtain the directions of least image diffusion (collinear with the fibres) [16–22]. Others transform the volume using Hough, Fourier, Radon, or similar approaches to detect the fibre directions and distributions [23–26]. A key advantage of these voxel-based methods is their ability to perform measurements on challenging or low resolution datasets where individual fibres are not distinguishable. Unfortunately, they usually lack the ability to treat fibres as separate entities.

In any case, once the fibre orientation can be determined, in-plane and out-plane misalignment angles can be obtained as $\alpha = \arctan\left(\frac{u}{l}\right)$ and $\beta = \arctan\left(\frac{v}{l}\right)$, respectively, where l is the distance between two consecutive slices (or samples), with u and v corresponding to the two out-plane and in-plane local displacement vectors [7,9,23,25,27,28]. From these, measures such as the severity factor [29], waviness, or
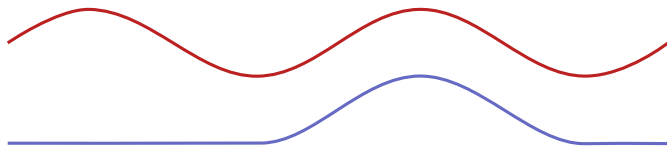

Fig. 1. Two fibres of similar scale, shape and length producing the same θ_{max} angle despite being different.

wavelength ratios [3,4,28,30–35] can be computed. These approaches have extensively been used to evaluate the effect of misalignments to mechanical properties. They have been applied not only on μCT data but also on other imaging modalities such optical microscopy [12, 23,25]. Despite its advantages, most approaches reduce the 3D fibre information to 2D counterparts by emphasizing on the angles or sinusoid shapes. However, as performed by [8] there is the possibility to consider a more fundamental measurement for 3D curves such as the Frenet–Serret [36,37] κ curvature formula. This approach assumes that each polygonal fibre of length l is a continuous function where at any arc-position location h a $\mathbf{P}_h$ point can be obtained by an $\mathbf{F}(h)$ interpolating function. In [8], fibre data obtained by the confocal laser scanning microscopy (CLSM) technique was fitted by polynomial space curves, from which the curvature of the fibres was derived. But as the greater the size of the data, the higher the degree of the polynomial curves, this approach is not suitable for high-resolution micro-computed tomography data. Building upon this continuous curvature definition, the first proposal of this paper is a new measurement to summarize the whole fibre into a single scalar which can serve as an indicator to determine the misalignments relevance.

Unfortunately, varying aspects such as the scale of imaged fibres, noise, resolution, sampling, etc. will have an impact on the measurements if these are directly computed over the input data. When one considers the fractal nature [38] of the noisy imaged fibres, then, a more finely sampled polygonal curve will inevitably consider more roughness and thus overestimate the measure. As this dependence on acquisition parameters is troublesome, a second proposal of this paper is a method to decouple it by smoothing the fibre trackings using a low-pass Gaussian convolution and binding its standard deviation σ parameter to the underlying dataset space units, i.e. nm, μm, etc. Note that most of the discussed methods, including the voxel-based ones do not take into account the aforementioned issue. Our approach overcomes these limitations by smoothing and interpolating respect physical space units, to achieve a decoupling from acquisition and/or reconstruction parameters.

The proposed measure and method have been tested using real and synthetic datasets to properly assess the behaviour and filtering capabilities. These synthetic cases were produced from exact definitions of curves swept using Gaussian splatters in order to generate slices mimicking real acquisition while controlling the morphological details from a signal processing point of view.

2. Material and methods

2.1. A new measure for waviness evaluation

As mentioned, the waviness of a 2D fibre $\mathbf{F}$ has been usually estimated by the maximum misalignment angle θ_{max} defined by:

$$\theta_{max} = \max_x \sphericalangle(\mathbf{F}'(x), \vec{i}),$$

where $\vec{i}$ represents the vector $(1, 0)$. However, in real composite materials, fibre-axis are ideally assumed to have a sinusoidal shape. That is, fibre-axes are modelled by

$$\mathbf{F}(x) = \left(x, A\sin\left(\frac{2\pi x}{\lambda}\right)\right) \quad x \in [0, \lambda],$$

where A and λ correspond the amplitude and wavelength, respectively. In this case, the waviness severity is measured by the ratio A/λ. Hsiao and Daniel in [31] made the following observation $\theta_{max} = \arctan(2\pi A/\lambda)$, and concluded that in unidirectional composites the major Young's modulus is severely degraded as the ratio A/λ increases. From this work, it can be derived that any measure of a fibre also increasing with respect to A/λ or θ_{max} (for instance), can be employed to assess the waviness severity. However, this θ_{max} parameter may not be sufficient to describe a fibre and its behaviour, sometimes, can be misleading.

For instance, in Fig. 1 the axes of two different fibres with the same θ_{max} are illustrated, however the blue one is less wavy than the red. Consequently, it seems necessary to make use of more geometric parameters to obtain a real description of the fibre characteristics. For this reason, in order to obtain a new measure of the waviness we propose using the total curvature K along the fibre as in Eq. (1), and then study how it is related with the θ_{max} parameter.

$$K = \int_{\mathbf{F}} \kappa \, d\mathbf{F} \tag{1}$$

First, let us study how the angle θ_{max} behaves under the assumption of a fibre shaped as a circular arc. In Fig. 2a one can observe that

$$\theta_{max} = \frac{l}{2R} = \frac{l}{2}\kappa,$$

with $\kappa = 1/R$ being the curvature of this circular arc. If this arc were to be composed by a finite number of sub-arcs of lengths l_i and central angles θ_i (see Fig. 2b), θ_{max} could be computed as follows:

$$\theta_{max} = \frac{1}{2}\sum_i \theta_i = \frac{1}{2}\sum_i l_i\kappa = \frac{1}{2}\int_0^l \kappa \, dh = \frac{K}{2}$$

Therefore, it seems that the total curvature is related with the fibre waviness severity. To further check this idea if we assume a fibre modelled by a sinusoid, the following must hold:

$$\mathbf{F}(x) = \left(x, A\sin\left(\frac{2\pi x}{\lambda}\right)\right), \qquad \mathbf{F}'(x) = \left(1, A\cos\left(\frac{2\pi x}{\lambda}\right)\frac{2\pi}{\lambda}\right),$$

$$\mathbf{F}''(x) = \left(0, -A\sin\left(\frac{2\pi x}{\lambda}\right)\left(\frac{2\pi}{\lambda}\right)^2\right).$$

Then,

$$\begin{aligned}
K &= \int_{\mathbf{F}} \kappa \, d\mathbf{F} = \int_0^\lambda \frac{|\det(\mathbf{F}'(x), \mathbf{F}''(x))|}{\|\mathbf{F}'(x)\|^3}\|\mathbf{F}'(x)\|dt \\
&= 2\int_0^{\lambda/2} \frac{A\sin\left(\frac{2\pi x}{\lambda}\right)\left(\frac{2\pi}{\lambda}\right)^2}{1 + A^2\cos^2\left(\frac{2\pi x}{\lambda}\right)\left(\frac{2\pi}{\lambda}\right)^2}dx = 4\arctan\left(\frac{2\pi A}{\lambda}\right) = 4\theta_{max}.
\end{aligned}$$

So, if the fibre was made up of n periods of λ wavelength, we would have $K = 4n\theta_{max}$. In this way, the blue fibre in Fig. 1 would have waviness of $4\theta_{max}$, while the red one $8\theta_{max}$. For this reason, it can be
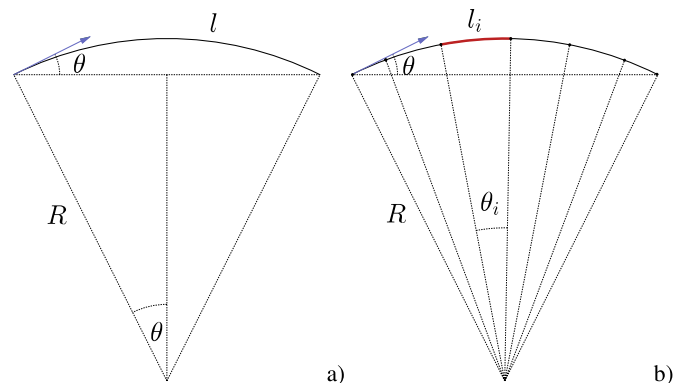

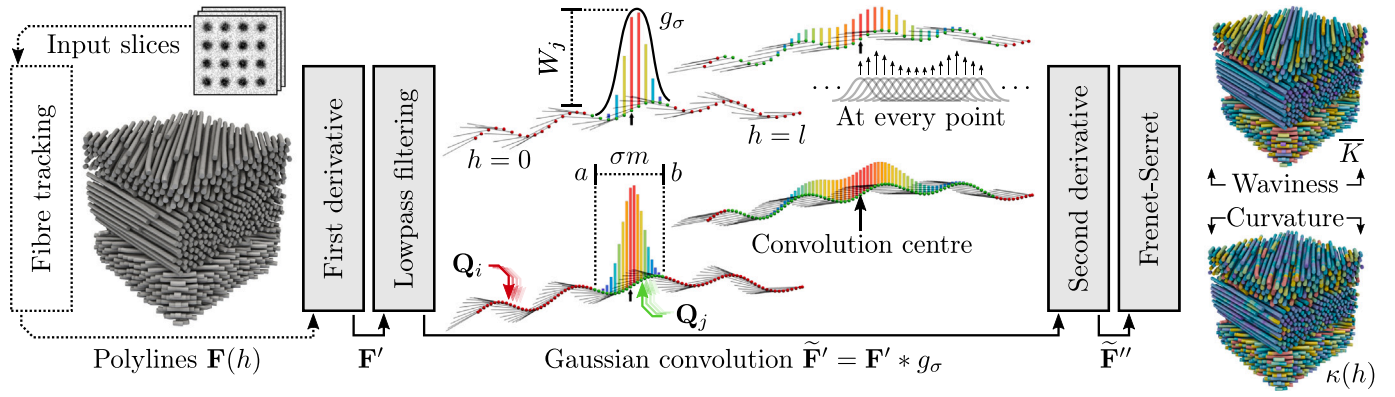**Fig. 2.** Maximum misalignment angle of a circular fibre arc.

Fig. 3. Method pipeline starting from the input slices (top left) up to the final measurements (right) with a detailed overview of the convolution state at two different σ and step sizes as seen from a single point (dark arrow) which is convolved according to the Gaussian distribution g_σ weights (coloured bars) until a σm distance (green dots) is reached. Fine black lines show the orientation of the first derivative. The curvature is computed for each fibre position (bottom right) or can be integrated into a single waviness scalar for the whole fibre (top right).

concluded, that the total curvature is a better descriptor of the waviness in fibres.

However, note that the fibres depicted in Fig. 1 have similar length. So, in order to produce a more intuitive scalar for the whole fibre indicating the waviness independently of the fibre length; we propose to consider the waviness as the average curvature $\overline{K}$ along the fibre, as in Eq. (2) where l corresponds to the fibre length.

$$\overline{K} = \frac{K}{l} = \frac{1}{l} \int_{\mathbf{F}} \kappa \, d\mathbf{F} \tag{2}$$

2.2. Algorithm

Given a set of polygonal trackings representing real fibres we want to obtain a continuous curvature indicator κ along the fibre, and a single K waviness scalar summarizing the whole fibre itself. To compute these, as illustrated in Fig. 3 (dashed box), a preliminary step to reconstruct the fibres to polygonal paths is required. Although different methods can be applied, in our case we used the Julià et al. [16] method. This considers the input volume as a whole, employs an uniformly behaving 3D reconstruction algorithm, and is capable of seamlessly tracking complex curves using variable step sizes.

Irrespective to the reconstruction algorithm employed, the method assumes the input fibres as a set of 3D curve functions, each independently represented by a chain of irregularly sampled points $\{\mathbf{Q}_0, \ldots, \mathbf{Q}_i, \ldots, \mathbf{Q}_n\}$ conforming a path of $n-1$ linked segments up to length of l space units mapped by a function $\mathbf{F}$ which given a parametric coordinate $h \in [0, l]$ produces an interpolated $\mathbf{F}(h)$ point between the neighbouring $\mathbf{Q}_i$ samples. In what follows, h_i will denote the arc-position parameter snapped to a discrete sample, thus satisfying $\mathbf{F}(h_i) = \mathbf{Q}_i$. With these definitions, the curvature at any position $\mathbf{F}(h)$ in a fibre can be defined by the κ parameter extracted using the Frenet–Serret formulas [36,37] as in Eq. (3). Moreover, the average curvature $\overline{K}$ along the fibre, that is, the new measure of the waviness proposed, can be computed as in Eq. (4).

$$\kappa(h) = \frac{\|\mathbf{F}'(h) \times \mathbf{F}''(h)\|}{\|\mathbf{F}'(h)\|^3} \tag{3}$$

$$\overline{K} = \frac{1}{l} \int_0^l \kappa(h) \|\mathbf{F}'(h)\| \, dh \tag{4}$$

Note that these measures, if applied directly, will overestimate the results depending on undesired factors such as the input volume noise level, sampling, etc. For this reason, as illustrated in Fig. 3 (filled grey boxes) the following four steps are applied: (i) the first derivative is computed; (ii) curvatures below a certain size are attenuated; (iii) the second derivative is computed; and (iv) the aforementioned curvature and waviness formulas are calculated for every tracked fibre. In the next sections we describe each one in more detail.

2.2.1. First derivative (tangent vector)

The algorithm begins by computing at each discrete $\mathbf{Q}_i$ sample an approximation $\mathbf{F}'(h_i)$ of the first derivative respect the arc distance h in space units. When three samples are available (i.e. $0 < i < n$), the first derivative at h_i is computed using the second order Lagrange interpolating polynomial using the pairs $(h_{i-1}, \mathbf{Q}_{i-1})$, $(h_i, \mathbf{Q}_i)$ and $(h_{i+1}, \mathbf{Q}_{i+1})$. Otherwise, at $\mathbf{Q}_0$ and $\mathbf{Q}_n$ extremes, the approximation is similarly computed using two samples and a first order interpolating Lagrange polynomial. Note that the results of this step, despite being valid vary upon undesired external factors such as the volume resolution, fibre scale, sampling frequency (i.e. step size), etc.

2.2.2. Low-pass filtering

As ignoring the aforementioned externalities will lead to ill-formed measurements, the first derivative is convolved (Eq. (6)) using a Gaussian distribution (Eq. (5)) whose σ parameter smoothly adjusts (in space units) the scale below which perturbations and thus high frequency information shall be attenuated, and thus decoupled from the underlying sampling and/or acquisition parameters.

$$g_\sigma(x) = \frac{1}{\sigma\sqrt{2\pi}} e^{-\frac{x^2}{2\sigma^2}} \tag{5}$$

$$\widetilde{\mathbf{F}}'(h) = \mathbf{F}' * g_\sigma = \int_{-\infty}^{+\infty} \mathbf{F}'(s) \, g_\sigma(s-h) \, ds \tag{6}$$

This smoothed derivative $\widetilde{\mathbf{F}}'$ needs to be approximated at each discrete sample $\mathbf{Q}_i$. To do this, the integration interval (i.e. convolution window size) is restricted to have at most a reach of σm space units, with the m parameter being a user-adjustable setting trading off performance versus accuracy. In parametric coordinates, this $[a, b]$ interval is determined by:

$$a = \max\left(0, h_i - \frac{\sigma m}{2}\right), \qquad b = \min\left(l, h_i + \frac{\sigma m}{2}\right).$$

Then, for each discrete sample $\mathbf{Q}_j$ whose parameter h_j lies in $[a, b]$, a weight W_j is computed by:

$$W_j = \int_{\frac{h_{j-1}+h_j}{2}}^{\frac{h_j+h_{j+1}}{2}} g_\sigma(s-h_i) \, ds.$$

Finally, $\widetilde{\mathbf{F}}'(h_i)$ is approximated as follows in Eq. (7a). In addition, one can refer to Eq. (7b) for a more generalized definition.

$$\widetilde{\mathbf{F}}'(h_i) \simeq \frac{\sum_j \mathbf{F}'(h_j) W_j}{\sum_j W_j} \tag{7a}$$

$$\widetilde{\mathbf{F}}'(h_i) \simeq \frac{\int_a^b \mathbf{F}'(s-h_i) g_\sigma(s-h_i) \, ds}{\int_a^b g_\sigma(s-h_i) \, ds}, \quad ds = \text{variable step size} \tag{7b}$$
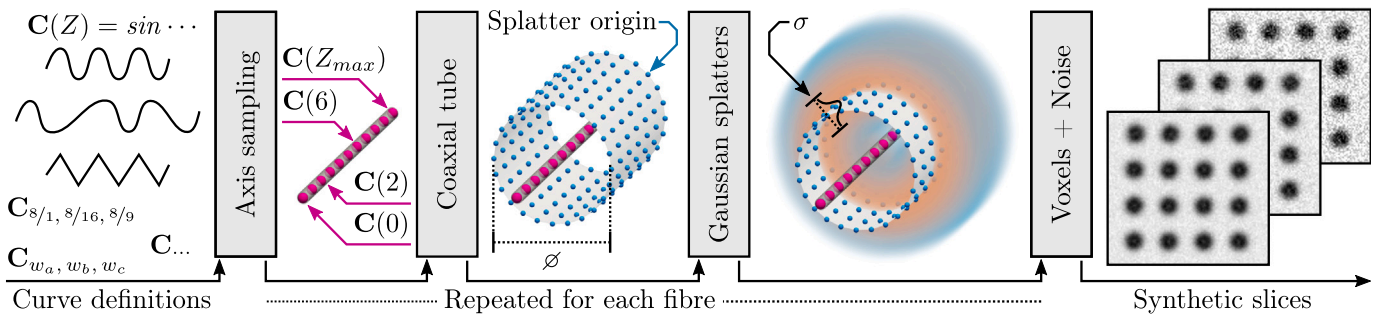
Fig. 4. Each curve definition is sampled at discrete points (magenta) which are then radiated outwards in order to produce a coaxial tube where at each of its surface vertex (blue) a Gaussian blur is splattered, and then sampled into the resulting synthetic slices (right).

Fig. 3 illustrates how the reach (green dots) and weights (bars) of the convolutions become independent from the underlying sampling. In addition the smoothing effect in tangent vectors (thin lines) when σ is increased can be observed by visually comparing between the four examples.

2.2.3. Second derivative (normal vector)

In this third step, and with the undesired high frequency information removed, the method proceeds to calculate the second derivative $\widetilde{\mathbf{F}}''(h_i)$ from the smoothed first derivative $\widetilde{\mathbf{F}}'(h_i)$ results by applying the same method explained in Section 2.2.1. Note that the normal vector produced will have an unstable direction when the fibre travels straight as illustrated by the ribbons normals in Fig. 6 (right) and Fig. 9 (bottom row).

2.2.4. Computing the curvature and waviness

In this last step, as our implementation employs the VTK (Visualization ToolKit) and each fibre is represented by a polyline, data values can be associated at two levels: (i) for every $\mathbf{Q}_i$ sample (point data), (ii) or to the whole line $\mathbf{F}$ (cell data). Consequently, the tangent $\widetilde{\mathbf{F}}'(h_i)$ and normal $\widetilde{\mathbf{F}}''(h_i)$ vectors are stored as point data, alongside the curvature measurement $\kappa(h)$ defined by Eq. (3) and computed as expressed by Eq. (8).

$$\kappa(h_i) = \frac{\|\widetilde{\mathbf{F}}'(h_i) \times \widetilde{\mathbf{F}}''(h_i)\|}{\|\widetilde{\mathbf{F}}'(h_i)\|^3} \qquad (8)$$

Finally, this point curvature can be integrated using the trapezoidal rule into a scalar summarizing the average waviness $\overline{K}$ (see Eq. (9)) and stored as cell data information (i.e. single value assigned to the whole fibre).

$$\overline{K} \simeq \frac{1}{h_n} \sum_{i=0}^{n-1} \frac{\kappa(h_i)\|\widetilde{\mathbf{F}}'(h_i)\| + \kappa(h_{i+1})\|\widetilde{\mathbf{F}}'(h_{i+1})\|}{2}(h_{i+1} - h_i) \qquad (9)$$

2.3. Experiments and testing datasets

The proposed method has been tested using the real *cfrp_i17* dataset with three straight fibre orientations and acquired with the European Synchrotron Radiation Facility's ID19 Beamline (ESRF, Grenoble) at 26 keV, and pixel size of 650 nm. It has been cropped in two different $250 \times 250 \times 250$ and $500 \times 500 \times 500$ sub-volumes named *cfrp250* and *cfrp500* respectively and made available in Supplementary Material 1. However, in order to properly assess the invariance and filtering capabilities of the proposed algorithms, six synthetic datasets named *harmonics*, *hifreq*, *mixed*, *polarized*, *helix*, and *helixnoise* have been generated in order to produce a set of complex fibre paths by morphing and combining characteristics (frequencies) at different scales.

2.3.1. Synthetic fibre generation

As illustrated by Fig. 4, synthetic datasets are generated using a three-phase process which begins by: (i) discretely mapping (in our case along the Z slicing axis) a medial axis curve $\mathbf{C}$ in order to obtain a finite set of high resolution points (pink dots); (ii) sweeping a coaxial tube around it to produce a new surface (white); and (iii) splatting Gaussian blurs of σ size at each surface vertex (blue dots). These steps are repeated for each input $\mathbf{C}$ such that a diffuse cloud of intensities is then quantized into a finite resolution volume where random white noise is mixed before producing the image slices. Depending on the relationship between the σ and the tube diameter $\varnothing$, the central intensity decay will be more or less accentuated; a useful feature mimicking beam-hardening artifacts [1] (Section 6.1).

2.3.2. Synthetic cases

With the ability to produce synthetic fibres from an exact $\mathbf{C}$ function, the next step is defining and arranging several of them in a volume. Most of our synthetic datasets are organized in 4 different blocks of 4×4 fibres, where each position corresponds to a unique combination of the three w_a, w_b, and w_c weighting variables in order to obtain 64 unique (but similar) $\mathbf{C}_{w_a, w_b, w_c}$ fibres exhibiting different amplitudes for each tunable feature. Every fibre function is sampled along the Z-axis, and shifted on the X-Y plane as illustrated in Fig. 5 in order to achieve the aforementioned arrangement. These volumes have a size of $512 \times 128 \times 512$ voxels and a dynamic range of 8 bits.

While all synthetic datasets can be expressed as a mathematical equation, the simpler *harmonics* case is expressed in Eq. (10) where a fibre combines three circular oscillations: (i) a lower frequency one, turning once from start to end; (ii) a mid frequency revolving twice; and (iii) a higher one oscillating four times. Each is respectively adjusted according to the w_a, w_b, and w_c weights and arranged in rows, columns and blocks as disposed in Fig. 5 obtaining a total of $4 \times 4 \times 4 = 64$ fibres as different 4 values for each weight are combined. In this way, one can easily analyse and isolate each variable; for instance, the effects of high frequencies are perceived observing the differences between blocks.

$$\mathbf{C}_{w_a, w_b, w_c}(z) = (0, 0, z) \quad + \quad (\sin(2\pi z/z_{max}), \cos(2\pi Z/Z_{max}), 0)\, w_a$$
$$+ \quad (\sin(4\pi z/Z_{max}), \cos(4\pi Z/Z_{max}), 0)\, w_b \quad ,$$
$$+ \quad (\sin(8\pi z/Z_{max}), \cos(8\pi Z/Z_{max}), 0)\, w_c$$

$$\begin{cases} w_{a,b,c} & \in \{8/1,\ 8/4,\ 8/9,\ 8/16\} \\ Z_{max} & = 512 \\ z & \in [0,\ Z_{max}] \end{cases} \qquad (10)$$

The *polarized* dataset is characterized by its oscillations in a single plane. It employs the same methodology for arranging the w_a, w_b, and w_c weights as in Fig. 5 in order to: (i) encode a lower frequency turn from start to end in the rows w_a; (ii) a high frequency (8 turns) in the columns w_b; and (iii) a Z-axis rotation of the oscillating plane between blocks w_c.
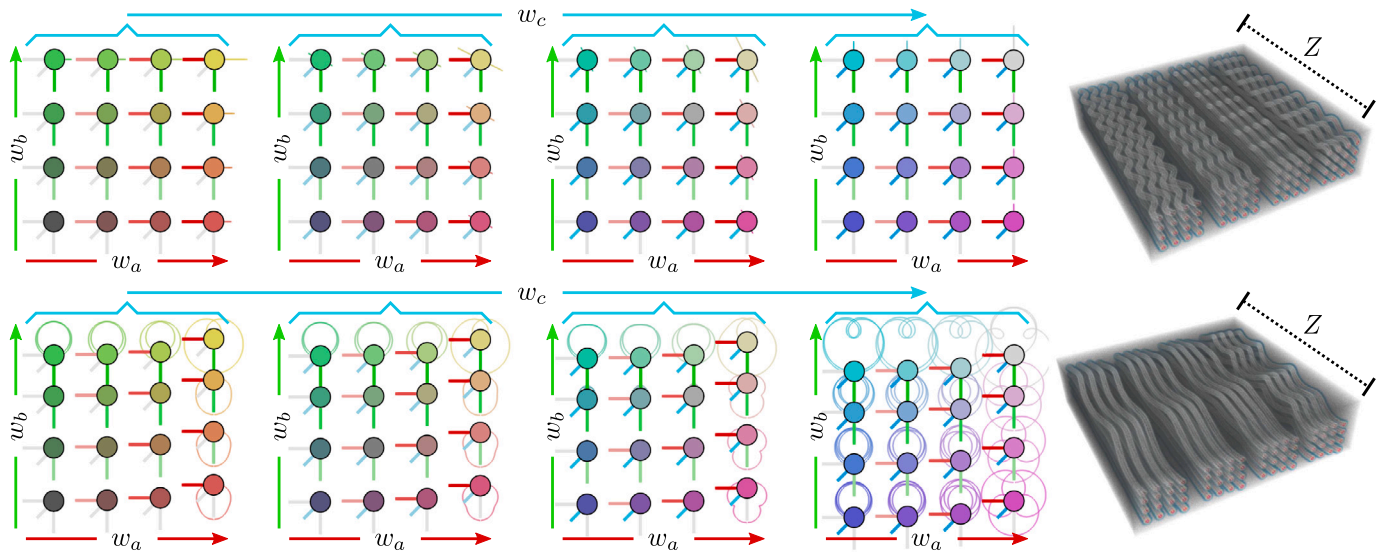
Fig. 5. Arrangement as seen from the X-Y plane of the three weighting variables: w_a (red, columns), w_b (green, rows), and w_c (blue, blocks); with circles colour-mapping them in RGB respectively; combined with an overlay and a thumbnail of the produced curves. The *polarized* (top) and *harmonics* (bottom) cases are illustrated.

The *hifreq* dataset reuses the same low w_a and mid w_b frequency components of the *harmonics* case, but regarding the very high frequency w_c feature varied for each block, is a more complex combination of circular and linear oscillations whose amplitude gradually decays to zero as one of the fibre extremes is reached. With it, the local curvature (i.e. point curvature) can be properly tested as is expected to significantly change within the polyline.

Complementing these, and in order to ease the posterior validation of the method, two datasets denominated *helix* and *helixnoise* were created from the single wavelength (i.e. only one frequency) functions Eq. (11a) and Eq. (11b) respectively. The latter raises the noise level by adding a uniform error of ± 2 to the X and Y medial-axis coordinates.

$$\mathbf{C}_{\text{helix}}(z) = \left(10\cos\left(\frac{20\pi z}{512}\right), \, 10\sin\left(\frac{20\pi z}{512}\right), \, z \right), \quad z \in [0, 512] \quad (11a)$$

$$\mathbf{C}_{\text{helixnoise}}(z) = \left(10\cos\left(\frac{20\pi z}{512}\right) + x_{\text{err}}(z), \, 10\sin\left(\frac{20\pi z}{512}\right) + y_{\text{err}}(z), \, z \right),$$

$$x_{\text{err}}(z), \, y_{\text{err}}(z) \sim U(-2, 2) \quad z \in [0, 512] \quad (11b)$$

Finally, the *mixed* dataset combines and exaggerates the features of the aforementioned cases in order to produce complex shapes at different scales.

3. Results and discussion

The proposed measurement algorithm has been implemented in C++ as the VTK [39] filter presented in Supplementary Material 2, which has been integrated in the Starviewer [40] platform as illustrated in Fig. 12. In Supplementary Material 1 the results, slices, figures, extra visualization, plots, and the code to produce the synthetic cases alongside its ground truth is made available to ensure the reproducibility.

3.1. Scale selectivity

A key distinctive feature of the proposed algorithm is its ability to suppress fibre variations below a certain size employing a low-pass Gaussian filter. Its behaviour is better understood when a **F** fibre curve is observed in the frequency space (i.e. Fourier-transformed) as a signal where high frequencies shall be eliminated. With the advantage of avoiding computationally intensive transformations; the Gaussian convolution employed behaves as a low-pass filter suppressing fibres below a user-specified σ wavelength in space units. These capabilities are demonstrated in Fig. 6 using the *hifreq* dataset containing an increasing amount finer variations at each block from left to right (refer to Section 2.3.2 and Fig. 5). When the σ parameter is smaller than the wavelength (first rows) the waviness measurements are distributed across blocks and the filter has little effect. But, as σ increases, as expected, these higher frequencies are attenuated, the waviness is decreased, and its relative distribution shifts from the blocks to the top rows (which have a mid-frequency). Then (in this example) at $\sigma > 30$, the lowest frequencies (columns) become more dominant and distinguishable.

If one observes the remaining comparative figures in Supplementary Material 1 the following key features of each dataset are fulfilled: (i) in *harmonics* a gradual and smooth transition from blocks to the upper-right corners where more curvature is present; (ii) in *polarized*, as expected the blocks present the same curvature, although with slight asymmetries in the intermediately rotated middle blocks; (iii) in *mixed* the desired selectivity is visually appreciated; and (iv) in the *crfp* cases, the outliers can be properly detected by their curvatures, and its main slightly curved regions can be identified at big σ values (see dashed circles in Fig. 9).

3.2. Definition of the signal and noise

From a signal processing perspective, the highest frequencies will not describe the actual shape of physical fibres, but instead manifest varying acquisition parameters such as voxel size, scale of the fibres, resolution, dynamic range, noise characteristics of the imaging device, etc. Hence, choosing a proper σ parameter to decouple these from our measurements is crucial to obtain comparable and non-overestimated measures across acquisitions. However, as illustrated in Fig. 6 (rows) and Fig. 3 (left vs right tangent thin lines) employing a σ well above the acquisition noise is also useful to discard smaller but physically present features from the curvature calculus. So, the σ parameter (arbitrarily set by the user) defines boundary between what shall be considered noise (higher frequencies), and signal (lower frequencies). As it specifies a wavelength in space units, it can be employed as an invariant reference value across different acquisitions. For these reasons, values below the sampling size and/or fibre diameter shall be discouraged.
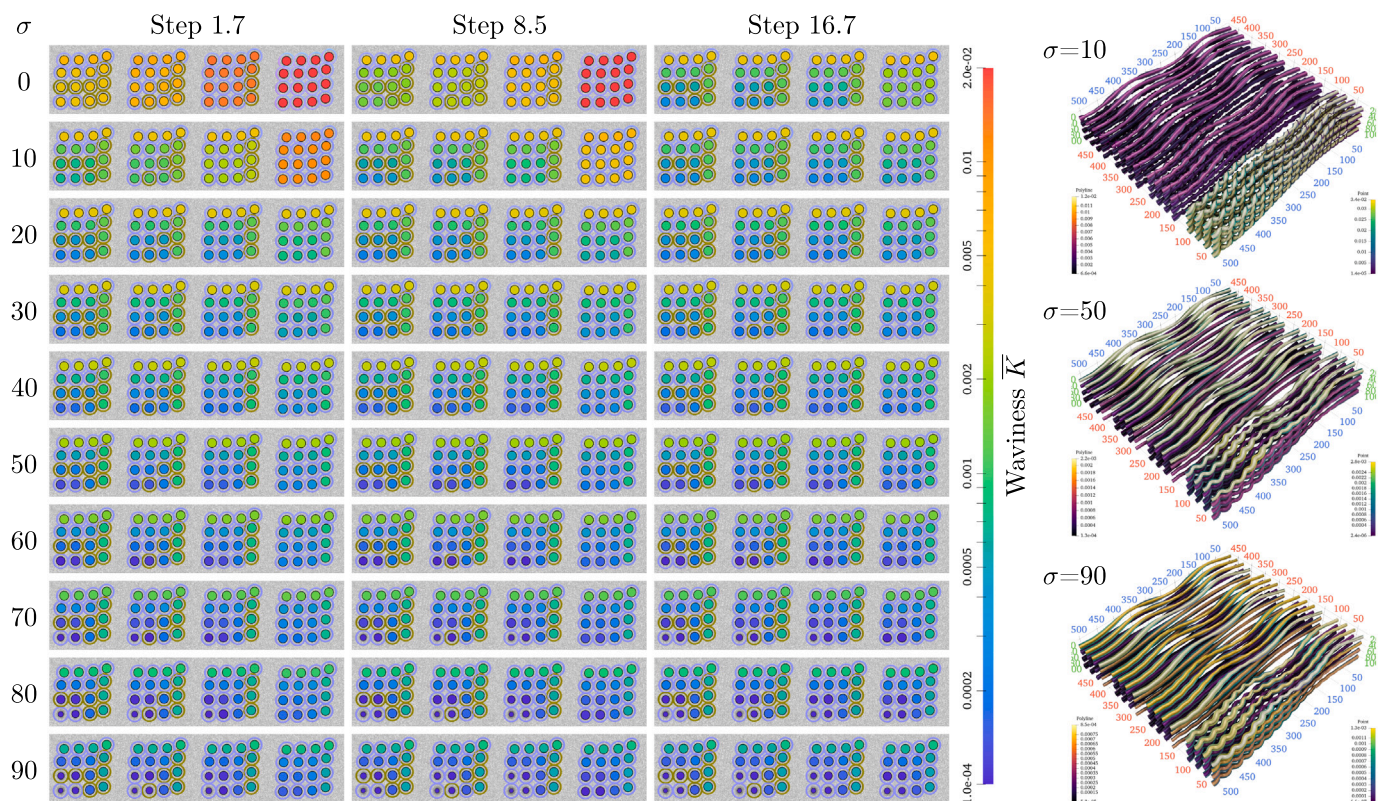
Fig. 6. On the right, a 3D visualization of the waviness (tube colour), normal vectors (ribbon orientation), and point curvature (ribbon colour) at three different σ values. On the left side, a matrix of slices comparing the waviness at different σ (rows) and sampling step sizes(columns). The waviness of each fibre (circle colour) is represented using the same scale to ease the comparison. Perimeter lines around circles RGB map the tangent vectors components.

3.3. Sampling

While the Gaussian convolution method is able to cut high frequencies, these must exist in the first place. In practice, fibres will never be infinitely sampled, consequently, they will be band-limited due to the Whittaker–Nyquist–Shannon sampling theorem [41–43]. This is an observable fact in Fig. 6 where the smaller σ in coarser cases do not have any effect until its value is greater than the sampling spacing. However, once exceeded, the curvature measurements converge irrespective of the sampling as illustrated by Fig. 8 with the values approaching to 1. In practice, these ratios arise from the median curvature of the 1.7 and 16.7 step size cases. In the employed Julià et al. [16] reconstruction method, steps sizes are user adjustable and may vary within a user-defined range. But, most reconstruction algorithms discussed in Section 1 implicitly set their sampling frequency by design choices such as snapping to integer voxel locations, reconstructing in a slice-by-slice approach, etc. In any case, all reconstruction methods, in addition to the ones performing measures voxel-wise, will have their highest frequencies capped according to the input volume resolution. However, relying on the sampling alone or other non-space referenced smoothing techniques (e.g. moving average of discrete samples) undermines the meaning of the measurement across different dataset acquisitions leading to a disparity in the results as observable in Fig. 7 when our method is set at $\sigma = 0$ (i.e. filtering disabled). For this reason, when one considers the fractal nature [38] of the noisy imaged fibres, then, a more finely sampled polygonal curve will inevitably consider more roughness and thus overestimate the measure.

3.4. Numeric stability and edge behaviour

One of the first aspects to consider is the finite lengths of the fibres; this approach was tackled by normalizing the vectors of the smoothed first derivatives in order to take in account the otherwise missing weight at the limits. Due to the nature of the curvature formula, its results are numerically stable even when a fibre travels straight (i.e. it also approaches zero), however, as future work we plan to further extend our measurements and provide more advanced visualizations. Also, relying on a pure Frenet–Serret frame is troublesome due to its abrupt changes in the normal vectors direction (see last row in Fig. 9). We plan to build upon slightly altered approaches such as [44] to mitigate these aforementioned issues, or by employing rotation minimizing frames such as [45].

3.5. Datasets and testing

The usage of datasets whose ground truths curves were analytically defined in terms of frequencies has been crucial to assess whether the theoretical expectations matched the actual measurements of the algorithm. Although these curves alone could have been directly fed into the measurement algorithm for testing purposes, this would have ignored the effect of white pixel noise, whose maximum frequency is in turn band-limited by the volume resolution. This noise affects the Julià et al. [16] tracking algorithm and it is manifested as small variations when a finer step size is employed (an expected behaviour). Despite the availability of datasets such as [6] with richer features better mimicking aspects such as beam hardening, we opted for a more conservative approach using Gaussian splatters in order to ensure an isotropic noise behaviour as the complex shapes are sampled into finite resolution slices. In addition to the volume and ground truths; in Supplementary Material 1 one will encounter the generative pipeline implemented in Paraview [46] to ensure the reproducibility by anybody and ease the creation of new datasets.

As illustrated in Fig. 9 visualizations, the method has been tested using a real dataset, and while the results and behaviour are coherent with synthetic cases, as future work we plan to extend the
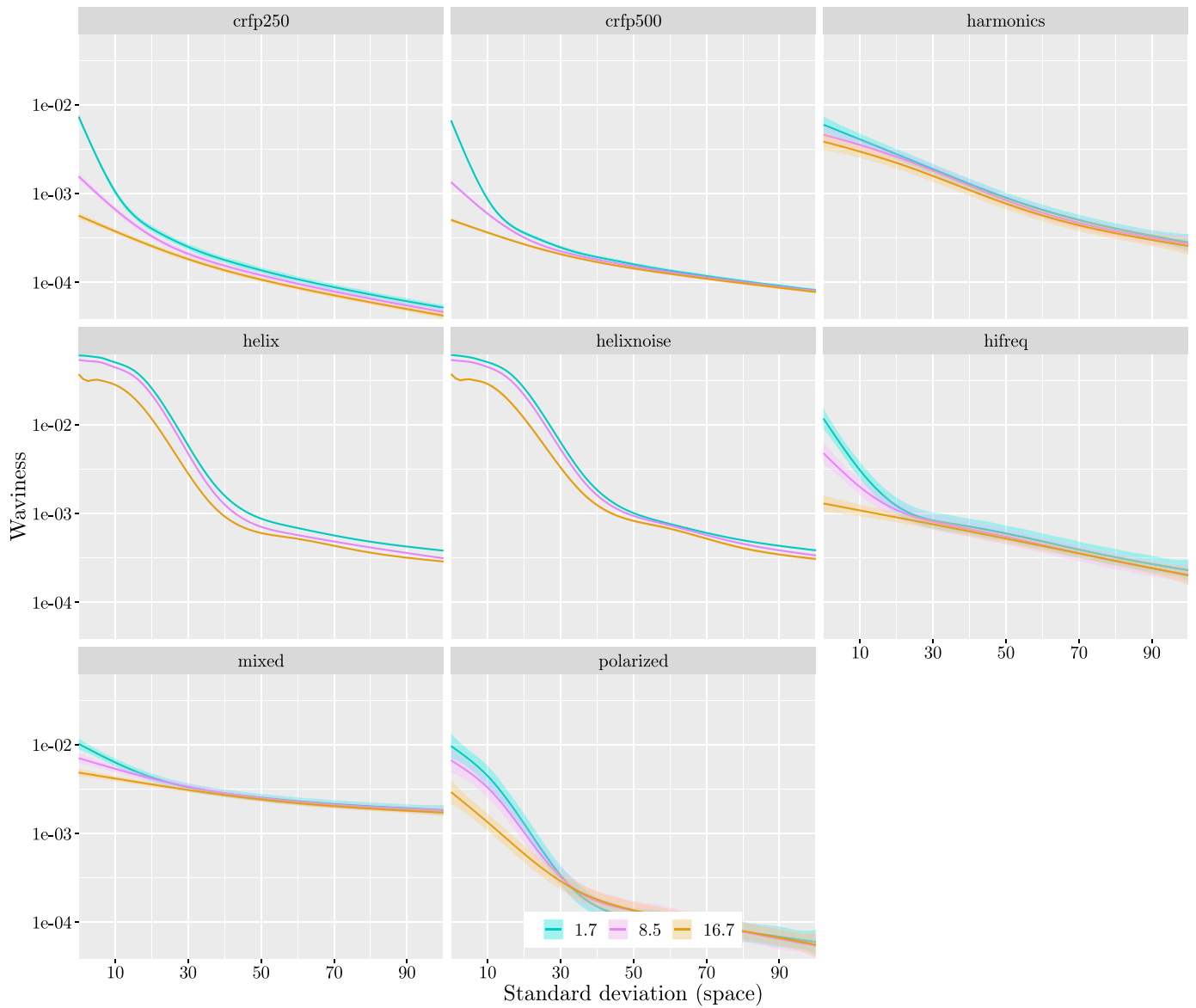
Fig. 7. For every dataset (boxes), a comparison of the mean waviness results (Log10 Y-axis) for each combination σ (X-axis) and step size (colours) values. Confidence intervals (semi-transparent colours) up to the 99th percentile.

testing by combining specimens with varied fibre diameters and altering acquisition parameters affecting resolution, contrast, noise levels, etc.

3.6. Validation

The implementation of the proposed algorithm can be validated against the simpler mathematical ground truth for the synthetic *helix* dataset of the unfiltered case (i.e. $\sigma = 0$) as expressed by Eq. (12) based on the fact that the curvature of a helix parameterized by $(A\cos(Bz), A\sin(z), z)$ is $AB^2/(1 + A^2B^2)$. The experimental results as shown in Table 1, indicate a deviation of just 0.6% respect the expected theoretical curvature, and while in the case of *helixnoise* slightly increases to 0.7%, the major differences regarding effects of noise are observable in the standard deviation. As illustrated in Figs. 10 and 11 the noise follows normal distribution which is narrowed and offset as the filtering sigma increases.

$$\kappa_{\text{helix}}(h_i) = \frac{AB^2}{1 + A^2B^2} \, , \quad A = 10 \, , \quad B = 20\frac{\pi}{512} \tag{12a}$$

$$\kappa_{\text{helix}}(h_i) = \frac{\pi^2 125}{\pi^2 1250 + 8192} \simeq 0.060095 \tag{12b}$$

3.7. Cost

The algorithm cost grows linearly respect the overall number of samples within a volume, but the amount of operations required at each one will depend on the amount of discrete neighbours convolved in a σm arc distance. While similar to discrete convolution kernels (e.g. Gaussian blur of an image), our kernel size cannot be precisely known nor allocated beforehand. As illustrated in Fig. 3, the active voxel (upwards black arrow) must access its discrete neighbours (green points) around a $\frac{\sigma m}{2}$ arc distance in space units. As by definition the spacing is irregular (even within a polyline), a reasonable way to quantify the cost is applying Eq. (13) using estimative averages of the fibre step sizes $\overline{ds}$, samples $\overline{n}$ and length $\overline{h}$.

$$\text{Operations per arc unit length} \simeq \frac{\overline{h}\sigma m}{\overline{n}\,\overline{ds}} \tag{13}$$
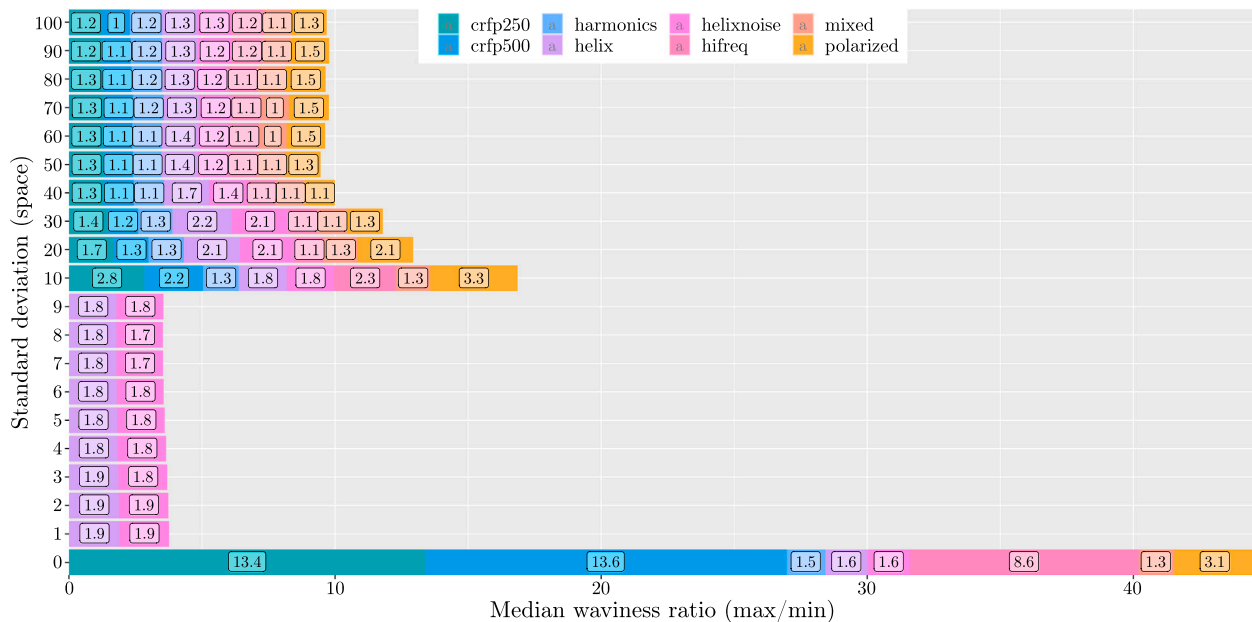
Fig. 8. For each case (colours), ratio (X-axis) between the maximum and minimum median values at different σ (Y-axis) of the whole volume waviness (labels, bar size) grouped by each step size tested. In practice, it is the ratio between the 1.7 and 16.7 steps sizes. Values approaching 1 indicate convergence of the measurement irrespective the sampling. Cases from $\sigma = 1$ to $\sigma = 9$ were only available for the *helix* and *helixnoise* datasets.
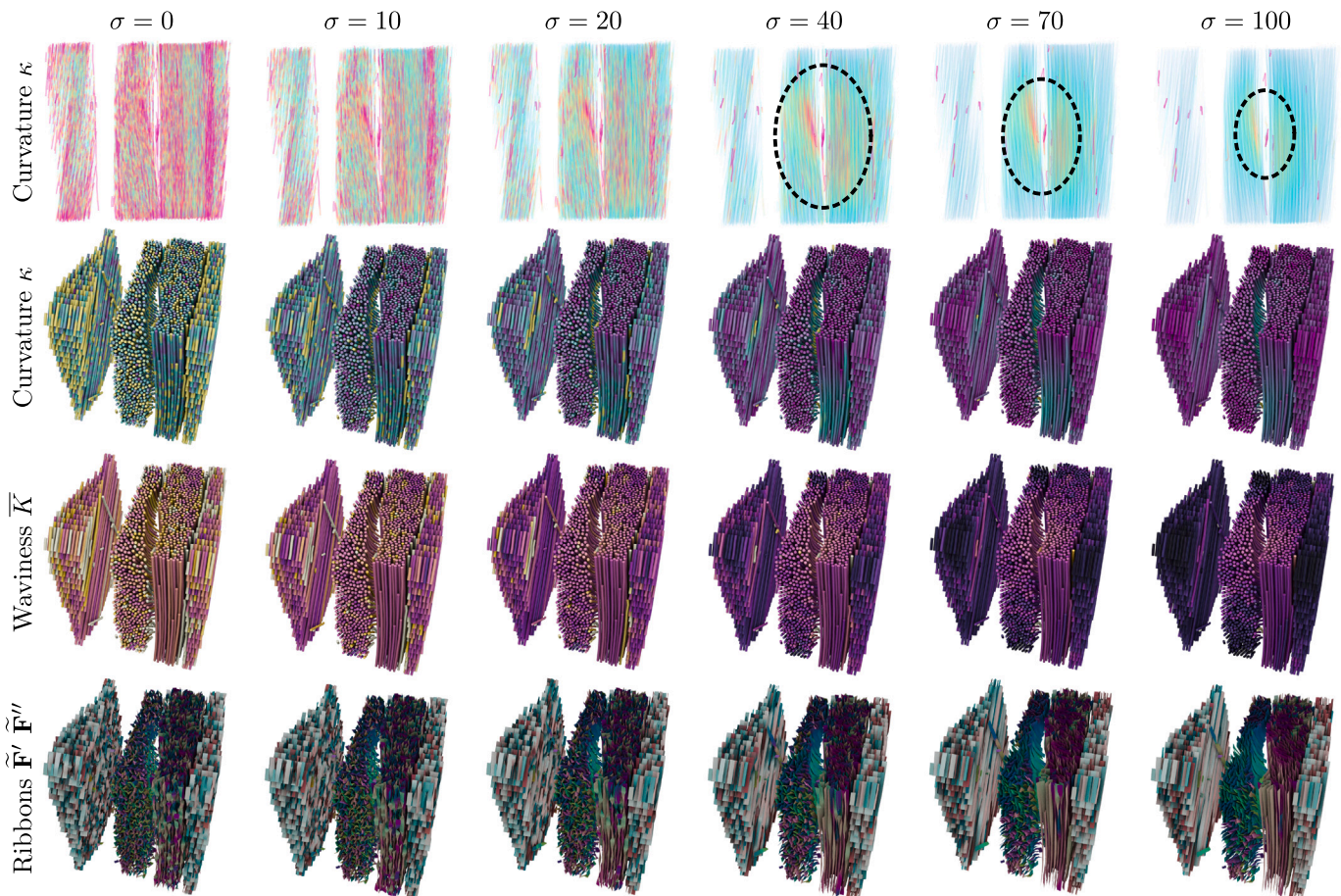

Fig. 9. Results and visualizations for the *crfp500* real dataset. Each column in the matrix corresponds to a different σ value. Colour scales are not rescaled within a row. The first row maps the curvature κ using semi-transparent lines; the second one also maps κ employing 3D tubes around the reconstructed curves; the third one maps the waviness $\overline{K}$ as a single colour for the whole fibre; and the last one employs ribbon surfaces to express the second derivative $\widetilde{\mathbf{F}}''$ orientation combined with an RGB colour mapping of the first derivative $\widetilde{\mathbf{F}}'$. The dashed circles pinpoint a properly identified region of interest where the curvature increases slightly.
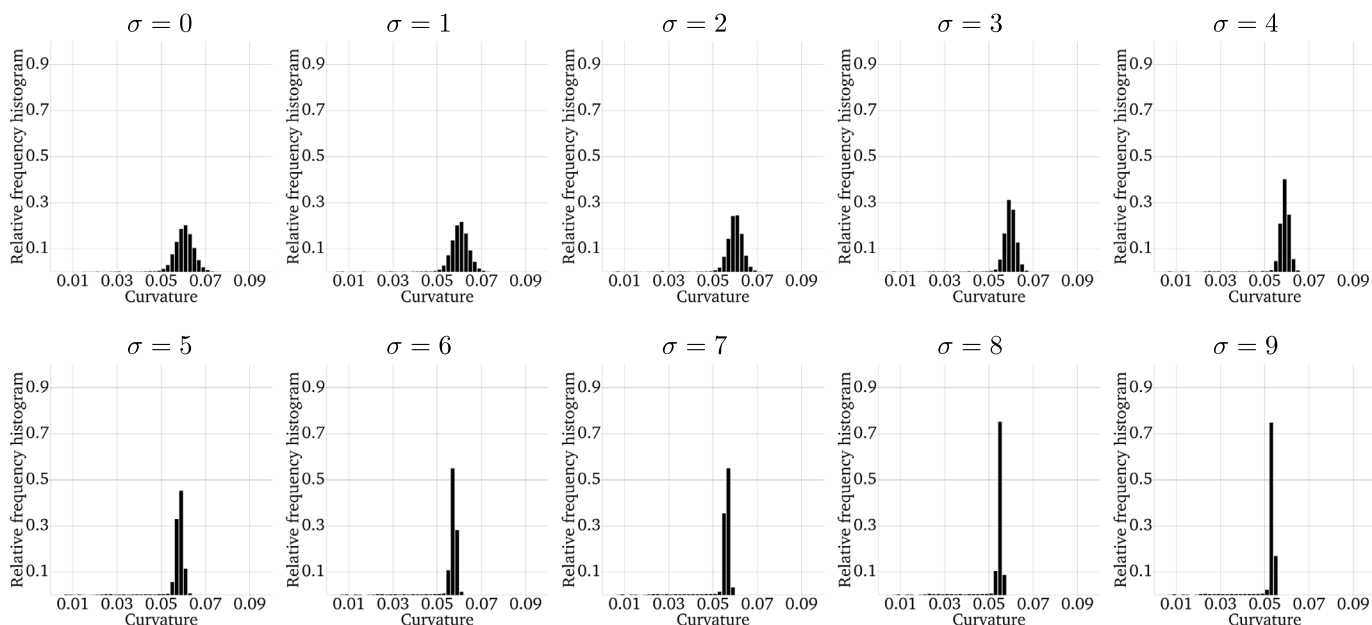
Fig. 10. Point curvature histograms of the *helix* dataset at different filtering levels (from $\sigma = 0$ to $\sigma = 9$) employing a fine 1.7 step size.
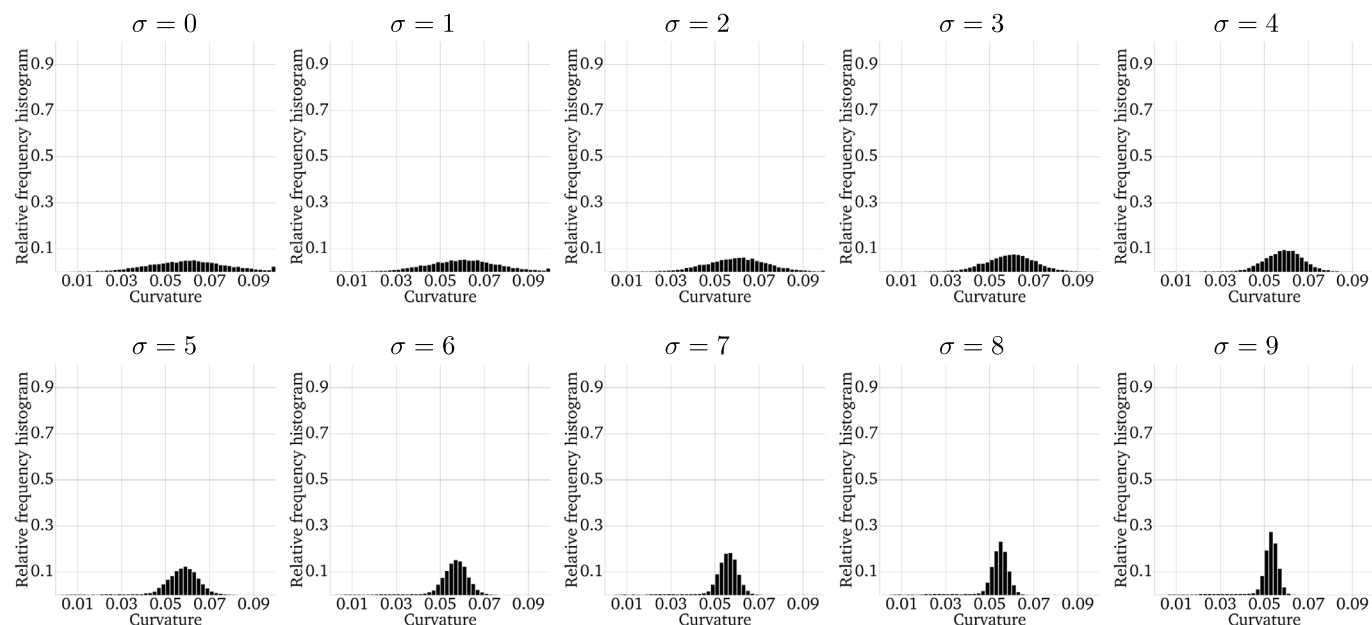

Fig. 11. Point curvature histograms of the *helixnoise* dataset at different filtering levels (from $\sigma = 0$ to $\sigma = 9$) employing a fine 1.7 step size.

While this linear behaviour is comparable to the more straightforward approaches discussed in Section 1, in practice, larger convolutions in our method will severely impact the runtime. However, with larger σ values respect the step size, one may voluntarily use coarser step sizes in order to reduce them, and thus indirectly prefilter the highest frequencies as discussed in Section 3.3. Finally, the implemented VTK filter in Supplementary Material 2, although useable, does not support multithreading yet, and as future work we plan to parallelize it at a fibre level, i.e. by polydata cells.

4. Conclusions

In this paper we have presented a method to assess the point curvature and overall waviness of fibres represented as polygonal curves

reconstructed from μCT slices. While the required input is independent respect the underlying tracking methodology, we used an inherently 3D one with the ability to produce irregularly spaced samples in order to ensure a high level of compatibility should any other state-of-the-art tracking method be used in-place.

Our Frenet–Serret based measurements ensure an inherent 3D behaviour which has been proven numerically stable for the measurement of fibre misalignments. Additionally it has the advantage of being a decoupled measure from the world-orientation of the dataset; in this way, there is no need to perform fine realignments to the specimens across acquisitions thus avoiding the introduction of further error. Also, we have demonstrated the relation of our proposal with common waviness measurements approaches which assume the fibres as simpler waveforms coplanar to a plane. This ability to address more complex cases with a more intuitive or expected behaviour makes our results

Table 1
Curvature statistics at different σ for the *helix* and *helixnoise* synthetic datasets.

| Case	σ	SD	Mean	Median
Helix	0	0.005252	0.060089	0.060466
Helix	1	0.005695	0.059847	0.060306
Helix	2	0.005625	0.059482	0.060033
Helix	3	0.005556	0.058945	0.059601
Helix	4	0.005545	0.058262	0.059014
Helix	5	0.005572	0.057400	0.058252
Helix	6	0.005597	0.056367	0.057336
Helix	7	0.005607	0.055152	0.056210
Helix	8	0.005588	0.053791	0.054918
Helix	9	0.005511	0.052192	0.053360
Helix	10	0.005370	0.050395	0.051584
Helixnoise	0	0.017702	0.060680	0.060499
Helixnoise	1	0.016580	0.060328	0.060512
Helixnoise	2	0.014307	0.059770	0.060193
Helixnoise	3	0.011831	0.059043	0.059700
Helixnoise	4	0.009813	0.058231	0.058941
Helixnoise	5	0.008365	0.057302	0.058100
Helixnoise	6	0.007407	0.056247	0.057052
Helixnoise	7	0.006787	0.055041	0.055901
Helixnoise	8	0.006372	0.053709	0.054629
Helixnoise	9	0.006044	0.052155	0.053125
Helixnoise	10	0.005745	0.050415	0.051431
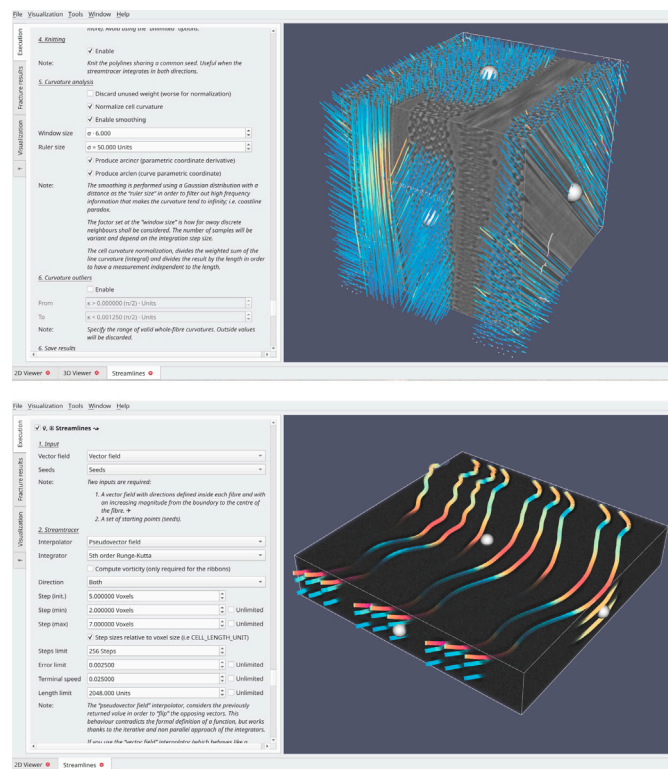
Fig. 12. The measurement method has been integrated in Starviewer [16,40]. All algorithm parameters are exposed to the end user (left sidepanels) who can later interactively explore and validate the results using fused volume renders of the underlying datasets. The *crfp500* (top) and *mixed* (bottom) cases are illustrated.

differ numerically from other measurements; however its mechanical implications can be deemed equivalent.

A key concept introduced in this paper is the importance of setting a limit to the smaller curvatures, and considering only the ones above a certain size. In our case, this scale selectivity is attained using a Gaussian low-pass frequency filter with an user-adjustable sigma parameter corresponding to a wavelength in space units. However, most state-of-the-art measurements in composite fibres ignore this fact, rely

only on the fibre resolution (i.e. sampling frequency) to limit the over-estimative effect of high frequencies, or may employ more advanced techniques, such as moving averages or polynomial interpolations not bound to actual space units making the results variant respect the acquisition parameters. Solving these issues and attaining coherent measurements across datasets can be challenging, especially with varying factors such as noise, resolution, sampling, etc. Our method attains convergence of results for fibres sampled at different resolutions when a sufficiently large sigma above the sampling frequency is employed. This adjustable low-pass filter, while a valuable tool to suppress the aforementioned fractality effects of high frequencies, can also be used to suppress smaller but undesired curvatures already present in the physical fibres deemed irrelevant for a particular case of study. Additionally, the algorithm has been validated against the mathematical ground truth (i.e. gold standard) which is properly matched by the experimental result when no smoothing is employed. Increasing the amounts of smoothing, as expected, the noise is reduced and the normal curvature distribution deviation narrowed. Smoothing values are recommended to be kept at least above 1 to 3 times the fibre diameter, taken to the extreme, the whole-volume curvature progressively decays to zero as all curvatures become suppressed. While advantageous, this effect must be considered and hence comparisons at different smoothing levels avoided as they are not directly comparable.

Although the behaviour is explainable by well established signal processing fundamentals, these have been experimentally tested using one real and several synthetic datasets. For this reason, we also introduced a methodology to generate synthetic volumes from a given ground truth defined as a composition of several oscillations. Although these synthetic slices do not reflect the richness of defects present in real acquisitions, their uniform behaviour and wave-based definition have been valuable tools to validate the theoretical expectations with actual results.

Our future work will be focused on further improving the algorithm performance and visualizations while combining it with other measurements employing rotation minimizing frames; performing the analysis at multiple scales; or expressing the curvature as an spectrum by binning the spectrum of spatial frequencies composing the fibre shapes.

CRediT authorship contribution statement

Declaration of competing interest

The authors declare that they have no known competing financial interests or personal relationships that could have appeared to influence the work reported in this paper.

Data availability

The data is made publicly available as supplementary materials files.

Acknowledgements

Appendix A. Supplementary data

1. **finalresults.tar.xz** Contains the code to generate synthetic volumes, the actual datasets, results for all tested combinations, code, figures, and extra visualizations.

   https://www.starviewer.org/papers/curvature/finalresults.tar.xz
   https://starviewer.udg.edu/papers/curvature/finalresults.tar.xz

   bfd6adba2867f5be0c5c4d3be54712503d931954024301727ef47173a2a22edb (SHA256)
   6d19e2a0b488713878781cfeeb304fffa3e59f4d (SHA1)

2. **vtkfilter.tar.xz** C++ code of the measurement algorithm implemented in the form of a VTK polydata filter. It is released under a BSD license compatible with VTK.

   https://www.starviewer.org/papers/curvature/vtkfilter.tar.xz
   https://starviewer.udg.edu/papers/curvature/vtkfilter.tar.xz

   096081b24182d6ef747d7a75079d196162cacec85d8548b91cd6a4db81b24649 (SHA256)
   07597a780286c2336eb6a41d27af1ee0b1b43503 (SHA1)

3. **video.mkv** Video of the implemented solution. The `.mkv` files are encoded in VP9 and contain a subtitle track with comments. We recommend visualizing them with https://www.videolan.orgVLC media player.

   https://www.starviewer.org/papers/curvature/video.mkv
   https://starviewer.udg.edu/papers/curvature/video.mkv

   d26304f991087a1a32bd63602b3da26857371f70231e54f64641eda60c756b58 (SHA256)
   b65a5960f37d478ca723bff7ecff823ddbcf22a2 (SHA1)

Supplementary material related to this article can be found online at https://doi.org/10.1016/j.measurement.2022.112223.

References

[1] J. Kruth, M. Bartscher, S. Carmignato, R. Schmitt, L. De Chiffre, A. Weckenmann, Computed tomography for dimensional metrology, CIRP Ann. 60 (2) (2011) 821–842, http://dx.doi.org/10.1016/j.cirp.2011.05.006, URL https://www.sciencedirect.com/science/article/pii/S0007850611002083.

[2] S. Garcea, Y. Wang, P. Withers, X-ray computed tomography of polymer composites, Compos. Sci. Technol. 156 (2018) 305–319, http://dx.doi.org/10.1016/j.compscitech.2017.10.023, URL https://www.sciencedirect.com/science/article/pii/S0266353817312460.

[3] P. Kulkarni, K.D. Mali, S. Singh, An overview of the formation of fibre waviness and its effect on the mechanical performance of fibre reinforced polymer composites, Composites A 137 (2020) 106013, http://dx.doi.org/10.1016/j.compositesa.2020.106013, URL https://www.sciencedirect.com/science/article/pii/S1359835X20302529.

[4] M. Alves, C. Cimini Junior, S. Ha, Fiber waviness and its effect on the mechanical performance of fiber reinforced polymer composites: An enhanced review, Composites A 149 (2021) 106526, http://dx.doi.org/10.1016/j.compositesa.2021.106526, URL https://www.sciencedirect.com/science/article/pii/S1359835X21002487.

[5] N.C. Davidson, A.R. Clarke, G. Archenhold, Large-area, high-resolution image analysis of composite materials, J. Microsc. 185 (2) (1997) 233–242, http://dx.doi.org/10.1046/j.1365-2818.1997.1560712.x, arXiv:https://onlinelibrary.wiley.com/doi/pdf/10.1046/j.1365-2818.1997.1560712.x.

[6] P.J. Creveling, W.W. Whitacre, M.W. Czabaj, A fiber-segmentation algorithm for composites imaged using X-ray microtomography: Development and validation, Composites A 126 (2019) 105606, http://dx.doi.org/10.1016/j.compositesa.2019.105606, URL https://www.sciencedirect.com/science/article/pii/S1359835X19303550.

[7] A. Clarke, G. Archenhold, N. Davidson, A novel technique for determining the 3D spatial distribution of glass fibres in polymer composites, Compos. Sci. Technol. 55 (1) (1995) 75–91, http://dx.doi.org/10.1016/0266-3538(95)00087-9, URL https://www.sciencedirect.com/science/article/pii/0266353895000879.

[8] A. Clarke, C. Eberhardt, The representation of reinforcing fibres in composites as 3D space curves, Compos. Sci. Technol. 59 (8) (1999) 1227–1237, http://dx.doi.org/10.1016/S0266-3538(98)00159-6, URL https://www.sciencedirect.com/science/article/pii/S0266353898001596.

[9] G. Requena, G. Fiedler, B. Seiser, P. Degischer, M. Di Michiel, T. Buslaps, 3D-quantification of the distribution of continuous fibres in unidirectionally reinforced composites, Composites A 40 (2) (2009) 152–163, http://dx.doi.org/10.1016/j.compositesa.2008.10.014, URL https://www.sciencedirect.com/science/article/pii/S1359835X08002662.

[10] R. Sencu, Z. Yang, Y. Wang, P. Withers, C. Rau, A. Parson, C. Soutis, Generation of micro-scale finite element models from synchrotron X-ray CT images for multidirectional carbon fibre reinforced composites, Composites A 91 (2016) 85–95, http://dx.doi.org/10.1016/j.compositesa.2016.09.010, URL https://www.sciencedirect.com/science/article/pii/S1359835X16303049.

[11] M.J. Emerson, K.M. Jespersen, A.B. Dahl, K. Conradsen, L.P. Mikkelsen, Individual fibre segmentation from 3D X-ray computed tomography for characterising the fibre orientation in unidirectional composite materials, Composites A 97 (2017) 83–92, http://dx.doi.org/10.1016/j.compositesa.2016.12.028, URL https://www.sciencedirect.com/science/article/pii/S1359835X16304560.

[12] D. Wilhelmsson, L. Asp, A high resolution method for characterisation of fibre misalignment angles in composites, Compos. Sci. Technol. 165 (2018) 214–221, http://dx.doi.org/10.1016/j.compscitech.2018.07.002, URL https://www.sciencedirect.com/science/article/pii/S0266353818309400.

[13] K. Amjad, W. Christian, K. Dvurecenska, M. Chapman, M. Uchic, C. Przybyla, E. Patterson, Computationally efficient method of tracking fibres in composite materials using digital image correlation, Composites A 129 (2020) 105683, http://dx.doi.org/10.1016/j.compositesa.2019.105683, URL https://www.sciencedirect.com/science/article/pii/S1359835X19304324.

[14] M. Mehdikhani, C. Breite, Y. Swolfs, M. Wevers, S.V. Lomov, L. Gorbatikh, Combining digital image correlation with X-ray computed tomography for characterization of fiber orientation in unidirectional composites, Composites A 142 (2021) 106234, http://dx.doi.org/10.1016/j.compositesa.2020.106234, URL https://www.sciencedirect.com/science/article/pii/S1359835X2030470X.

[15] C.N. Eberhardt, A.R. Clarke, Automated reconstruction of curvilinear fibres from 3D datasets acquired by X-ray microtomography, J. Microsc. 206 (1) (2002) 41–53, http://dx.doi.org/10.1046/j.1365-2818.2002.01009.x, arXiv:https://onlinelibrary.wiley.com/doi/pdf/10.1046/j.1365-2818.2002.01009.x.

[16] A. Julià i Juanola, M. Ruiz i Altisent, I. Boada i Oliveras, An efficient and uniformly behaving streamline-based μCT fibre tracking algorithm using volume-wise structure tensor and signal processing techniques, Comput. Methods Appl. Mech. Engrg. 394 (2022) 114898, http://dx.doi.org/10.1016/j.cma.2022.114898, URL https://www.sciencedirect.com/science/article/pii/S0045782522001359.

[17] Y.H. Lee, S.W. Lee, J.R. Youn, K. Chung, T.J. Kang, Characterization of fiber orientation in short fiber reinforced composites with an image processing technique, Mater. Res. Innov. 6 (2) (2002) 65–72, http://dx.doi.org/10.1007/s10019-002-0180-8.

[18] K. Robb, O. Wirjadi, K. Schladitz, Fiber orientation estimation from 3D image data: Practical algorithms, visualization, and interpretation, in: 7th International Conference on Hybrid Intelligent Systems (HIS 2007), 2007, pp. 320–325, http://dx.doi.org/10.1109/HIS.2007.26.

[19] M. Krause, J. Hausherr, B. Burgeth, C. Herrmann, W. Krenkel, Determination of the fibre orientation in composites using the structure tensor and local X-ray transform, J. Mater. Sci. 45 (2010) 888–896, http://dx.doi.org/10.1007/s10853-009-4016-4.

[20] I. Straumit, S.V. Lomov, M. Wevers, Quantification of the internal structure and automatic generation of voxel models of textile composites from X-ray computed tomography data, Composites A 69 (2015) 150–158, http://dx.doi.org/10.1016/j.compositesa.2014.11.016, URL https://www.sciencedirect.com/science/article/pii/S1359835X14003625.

[21] P. Pinter, S. Dietrich, B. Bertram, L. Kehrer, P. Elsner, K. Weidenmann, Comparison and error estimation of 3D fibre orientation analysis of computed tomography image data for fibre reinforced composites, NDT E Int. 95 (2018) 26–35, http://dx.doi.org/10.1016/j.ndteint.2018.01.001, URL https://www.sciencedirect.com/science/article/pii/S0963869517303821.

[22] R. Karamov, L.M. Martulli, M. Kerschbaum, I. Sergeichev, Y. Swolfs, S.V. Lomov, Micro-CT based structure tensor analysis of fibre orientation in random fibre composites versus high-fidelity fibre identification methods, Compos. Struct. 235 (2020) 111818, http://dx.doi.org/10.1016/j.compstruct.2019.111818, URL https://www.sciencedirect.com/science/article/pii/S0263822319322986.

[23] C. Creighton, M. Sutcliffe, T. Clyne, A multiple field image analysis procedure for characterisation of fibre alignment in composites, Composites A 32 (2) (2001) 221–229, http://dx.doi.org/10.1016/S1359-835X(00)00115-9, URL https://www.sciencedirect.com/science/article/pii/S1359835X00001159.

[24] R. Blanc, C. Germain, J.D. costa, P. Baylou, M. Cataldi, Fiber orientation measurements in composite materials, Composites A 37 (2) (2006) 197–206, http://dx.doi.org/10.1016/j.compositesa.2005.04.021, URL https://www.sciencedirect.com/science/article/pii/S1359835X05002472 CompTest 2004.

[25] K. Kratmann, M. Sutcliffe, L. Lilleheden, R. Pyrz, O. Thomsen, A novel image analysis procedure for measuring fibre misalignment in unidirectional fibre composites, Compos. Sci. Technol. 69 (2) (2009) 228–238, http://dx.doi.org/10.1016/j.compscitech.2008.10.020, URL https://www.sciencedirect.com/science/article/pii/S0266353808004132.

[26] T. Elberfeld, J. De Beenhouwer, A.J. den Dekker, C. Heinzl, J. Sijbers, Parametric reconstruction of glass fiber-reinforced polymer composites from X-ray projection data-A simulation study, J. Nondestruct. Eval. 37 (3) (2018) 62, http://dx.doi.org/10.1007/s10921-018-0514-0, URL https://europepmc.org/articles/PMC6314276.

[27] S. Yurgartis, Measurement of small angle fiber misalignments in continuous fiber composites, Compos. Sci. Technol. 30 (4) (1987) 279–293, http://dx.doi.org/10.1016/0266-3538(87)90016-9, URL https://www.sciencedirect.com/science/article/pii/0266353887900169.

[28] M. Sutcliffe, Modelling the effect of size on compressive strength of fibre composites with random waviness, Compos. Sci. Technol. 88 (2013) 142–150, http://dx.doi.org/10.1016/j.compscitech.2013.09.002, URL https://www.sciencedirect.com/science/article/pii/S0266353813003552.

[29] J. Wang, K. Potter, K. Hazra, M. Wisnom, Experimental fabrication and characterization of out-of-plane fiber waviness in continuous fiber-reinforced composites, J. Compos. Mater. 46 (17) (2012) 2041–2053, http://dx.doi.org/10.1177/0021998311429877.

[30] D. Liu, N. Fleck, M. Sutcliffe, Compressive strength of fibre composites with random fibre waviness, J. Mech. Phys. Solids 52 (7) (2004) 1481–1505, http://dx.doi.org/10.1016/j.jmps.2004.01.005, URL https://www.sciencedirect.com/science/article/pii/S0022509604000110.

[31] H. Hsiao, I. Daniel, Effect of fiber waviness on stiffness and strength reduction of unidirectional composites under compressive loading, Compos. Sci. Technol. 56 (5) (1996) 581–593, http://dx.doi.org/10.1016/0266-3538(96)00045-0, URL https://www.sciencedirect.com/science/article/pii/0266353896000450.

[32] L. Bloom, J. Wang, K. Potter, Damage progression and defect sensitivity: An experimental study of representative wrinkles in tension, Composites B 45 (1) (2013) 449–458, http://dx.doi.org/10.1016/j.compositesb.2012.05.021, URL https://www.sciencedirect.com/science/article/pii/S1359836812003472.

[33] K. Potter, B. Khan, M. Wisnom, T. Bell, J. Stevens, Variability, fibre waviness and misalignment in the determination of the properties of composite materials and structures, Composites A 39 (9) (2008) 1343–1354, http://dx.doi.org/10.1016/j.compositesa.2008.04.016, URL https://www.sciencedirect.com/science/article/pii/S1359835X08001176.

[34] K. Mizukami, Y. Mizutani, K. Kimura, A. Sato, A. Todoroki, Y. Suzuki, Y. Nakamura, Visualization and size estimation of fiber waviness in multidirectional CFRP laminates using eddy current imaging, Composites A 90 (2016) 261–270, http://dx.doi.org/10.1016/j.compositesa.2016.07.008, URL https://www.sciencedirect.com/science/article/pii/S1359835X16302287.

[35] M. Thor, U. Mandel, M. Nagler, F. Maier, J. Tauchner, M. Sause, R. Hinterhoelzl, Numerical and experimental investigation of out-of-plane fiber waviness on the mechanical properties of composite materials, Int. J. Mater. Form. 14 (2021) http://dx.doi.org/10.1007/s12289-020-01540-5.

[36] J.-A. Serret, Sur quelques formules relatives à la théorie des courbes à double courbure, J. Math. Pures Appl. (1851) 193–207, URL http://eudml.org/doc/235002.

[37] F. Frenet, Sur les courbes à double courbure., J. Math. Pures Appl. (1852) 437–447, URL http://eudml.org/doc/233946.

[38] B. Mandelbrot, How long is the coast of britain? Statistical self-similarity and fractional dimension, Science 156 (3775) (1967) 636–638, http://dx.doi.org/10.1126/science.156.3775.636, arXiv:https://www.science.org/doi/pdf/10.1126/science.156.3775.636.

[39] Kitware Inc., The visualization ToolKit, 2022, URL Internet.

[40] M. Ruiz i Altisent, A. Julià i Juanola, I. Boada i Oliveras, Starviewer and its comparison with other open-source DICOM viewers using a novel hierarchical evaluation framework, Int. J. Med. Inf. 137 (2020) 104098, http://dx.doi.org/10.1016/j.ijmedinf.2020.104098, URL https://www.sciencedirect.com/science/article/pii/S1386505619301108.

[41] E. Whittaker, XVIII.—On the functions which are represented by the expansions of the interpolation-theory, Proc. Roy. Soc. Edinburgh 35 (1915) 181–194, http://dx.doi.org/10.1017/S0370164600017806.

[42] H. Nyquist, Certain topics in telegraph transmission theory, Trans. Am. Inst. Electr. Eng. 47 (2) (1928) 617–644, http://dx.doi.org/10.1109/T-AIEE.1928.5055024.

[43] C. Shannon, Communication in the presence of noise, Proc. IRE 37 (1) (1949) 10–21, http://dx.doi.org/10.1109/JRPROC.1949.232969.

[44] J. Velut, A spline-driven image slicer, VTK J. (2011) http://dx.doi.org/10.54294/tih9wh, URL http://hdl.handle.net/10380/3318.

[45] W. Wang, B. Jüttler, D. Zheng, Y. Liu, Computation of rotation minimizing frames, ACM Trans. Graph. 27 (1) (2008) http://dx.doi.org/10.1145/1330511.1330513.

[46] Kitware Inc., ParaView, 2022, URL Internet.